

The orbital parameters of the gamma-ray binary LMC P3[★]

B. van Soelen,¹ † N. Komin,² ‡ A. Kniazev^{3,4}, P. Väisänen^{3,4}

¹Department of Physics, University of the Free State, PO Box 339, Bloemfontein 9300, South Africa

²School of Physics, University of the Witwatersrand, 1 Jan Smuts Avenue, Braamfontein, Johannesburg, 2050 South Africa

³South African Astronomical Observatory, PO Box 9, Observatory, 7935, Cape Town, South Africa

⁴Southern African Large Telescope, PO Box 9, Observatory, 7935, Cape Town, South Africa

Accepted XXX. Received YYY; in original form ZZZ

ABSTRACT

LMC P3 is the most luminous gamma-ray binary discovered to date and the first detected outside of the Galaxy, with an orbital period of 10.301 d. We report on optical spectroscopic observations undertaken with the Southern African Large Telescope (SALT) using the High Resolution spectrograph (HRS). We find the binary is slightly eccentric, $e = 0.40 \pm 0.07$, and place the time of periastron at $\text{HJD } 2457412.13 \pm 0.29$. Stellar model fitting finds an effective temperature of $T_{\text{eff}} = 36351 \pm 53$ K. The mass function, $f = 0.0010 \pm 0.0004 M_{\odot}$, favours a neutron star compact object. The phases of superior and inferior conjunctions are 0.98 and 0.24, respectively (where phase 0 is at the *Fermi*-LAT maximum), close to the reported maxima in the GeV and TeV light curves.

Key words: Gamma rays: stars; binaries: spectroscopic; Stars: massive; stars: neutron

1 INTRODUCTION

Gamma-ray binaries are a distinct class of high mass binary systems, defined by having spectral energy distributions that peak (in a νF_{ν} distribution) in the gamma-ray regime (see e.g. [Dubus 2013](#), for a detailed review of these sources). There are only seven such systems known, the most recent of which, PSR J2032+4127, was recently detected at very high energies around periastron in November 2017 ([Ho et al. 2017](#); [Mirzoyan & Mukherjee 2017](#); [The VERITAS Collaboration et al. 2018](#)). In this paper we present high resolution spectroscopic optical observations of the recently discovered source LMC P3, the most luminous of the gamma-ray binaries and the first detected outside of the Galaxy, lying in the Large Magellanic Cloud (LMC; [Corbet et al. 2016](#)).

All gamma-ray binaries consist of a compact object, within the mass range of a neutron star or a black hole, which is in orbit around an O or B type star ([Dubus 2013](#); [Corbet et al. 2016](#)). However, for only two systems, PSR B1259–63/LS 2883 and the recently detected PSR J2032+4127, is the nature of the compact known, since they have been detected as pulsars ([Johnston et al. 1992](#);

[Abdo et al. 2009](#)). In these systems, the non-thermal emission is believed to arise due to the particle acceleration that occurs at the shock that forms between the pulsar and stellar winds. In the other sources a black hole compact object cannot be ruled out, and microquasar scenarios are still considered.

LMC P3 was a point-like source “P3” detected in *Fermi*-LAT observations of the LMC ([Ackermann et al. 2016](#)). The binary nature of LMC P3 was discovered through a search for periodicity in *Fermi*-LAT observations, finding a 10.301 ± 0.002 d period ([Corbet et al. 2016](#)). LMC P3 is associated with the previously detected point-like X-ray source CXOU 053600.0–673507 located in the supernova remnant DEM L241 ([Bamba et al. 2006](#)). It was previously suggested by [Seward et al. \(2012\)](#) that based on the variability of the X-ray flux and small variations of the radial velocity of an O5III(f) star ($V = 13.5$) coincident with this X-ray source, that the object was a High-Mass X-ray Binary (HMXB) with a period of tens of days. X-ray and radio observations confirmed the multi-wavelength modulation on the same 10.301 d period while optical radial velocity measurements of the O5III(f) star (the earliest type of any gamma-ray binary) also showed a variation consistent with this period ([Corbet et al. 2016](#)). The binary solution to the radial velocities found a mass function of $f(M) = \left(1.3^{+1.1}_{-0.6}\right) \times 10^{-3} M_{\odot}$, however, the eccentricity of the system could not be constrained.

The radio and X-ray light curves are in phase, but are

[★] Based on observations made with the Southern African Large Telescope (SALT) under program 2016-1-MLT-006 (PI: N. Komin).

† E-mail: vansoelenb@ufs.ac.za

‡ E-mail: nukri.komin@wits.ac.za

in anti-phase with the *Fermi*-LAT light curves (Corbet et al. 2016). The H.E.S.S. telescope has subsequently reported detection at TeV energies (though only in a single phase bin) which is also in anti-phase with the *Fermi*-LAT observations (HESS Collaboration et al. 2018). This is very similar to what is observed for the gamma-ray binary LS 5039 (Aharonian et al. 2005; Kishishita et al. 2009; Abdo et al. 2009). Key to understanding the gamma-ray emission is obtaining a clear solution for the binary parameters of the source. Here we report on optical spectroscopic observations of LMC P3 undertaken with the Southern African Large Telescope (SALT) using the High Resolution spectrograph (HRS), to establish the binary parameters.

2 OBSERVATIONS

2.1 Observations and data reduction

LMC P3 was successfully observed 24 times with the High Resolution Spectrograph (HRS; Bramall et al. 2010, 2012; Crause et al. 2014) on the Southern African Large Telescope (SALT; Buckley et al. 2006) between 2016 September 14 and 2017 February 06.

The HRS is a dual-beam fibre-fed échelle spectrograph, housed within a vacuum tank, inside a thermo-stable room. The HRS is designed for extra-solar planet searches with velocity accuracies of 5 ms^{-1} in the High Stability Mode. As part of the HRS calibration plan, flats and ThAr hollow-cathode lamp spectra are obtained weekly through both the object and sky fibres. Observations of radial velocity standards are taken as part of the HRS calibration plan.¹

Observations were undertaken using the Low Resolution Mode ($R = 14000$), with each observation consisting of two camera exposures of 1220 s, (except for two nights where the exposure was increased to 2×1640 s). The different orders of the HRS spectra were extracted and wavelength calibrated using the HRS pipeline discussed in Kniazev et al. (2016). Each individual order of the spectrum was normalized and merged into a single one dimension spectrum using the standard IRAF/PyRAF packages. Heliocentric correction was performed for each individual exposure using RVCORRECT/DOPCOR and then nightly observations were averaged together.

HRS observations are undertaken with a $2.2''$ fibre placed on the target and a separate “sky fibre” that must be placed at least $16''$ away from the target. Because the target lies within a nebula the sky lines are dominated by the Balmer emission lines arising from the nebula, and the background sky measured in the sky fibre was significantly different from the sky as measured at the target. As a result, the sky subtraction was not able to properly correct for the nebula emission and introduced more noise into the spectrum. For this reason, no sky subtraction was performed and the analysis was restricted to the “blue” arm of the HRS where the nebula and sky contamination was minimal.

¹ The full details of the calibration plan and the stability of the radial velocity determinations are given in the SALT proposal call documentation http://pysalt.salt.ac.za/proposal_calls/current/ProposalCall.html.

2.2 Radial velocity determination

The radial velocity was investigated by fitting the position of individual lines and by cross-correlating the spectrum to a template.

The observed central wavelength of different absorption lines was determined by fitting Gaussian profiles, which showed that different line species have different radial velocities. This effect has previously been noted in O-type stars, and is most likely due to the contamination by the stellar wind (see e.g. Casares et al. 2005; Sarty et al. 2011; Puls et al. 1996; Waisberg & Romani 2015).

Because of the different velocities found for different lines the radial velocity was determined by cross-correlating individual spectra to a template, using the RVSAO/XCSAO package (Kurtz & Mink 1998). We followed a similar process to that described in, for example, Manick et al. (2015); Foellmi et al. (2003); Monageng et al. (2017), and created the template from the available observations. To create the reference template, first an average of all observations was found and the velocity shift between each observation and the average spectrum was determined through cross-correlation. Next, all the individual spectra were corrected by the shift to the average spectrum and the template was produced by averaging these velocity corrected spectra. The final template spectrum, in the $4150\text{--}4600 \text{ \AA}$ wavelength range used for the cross-correlation, is shown in Fig. 1.

In order to determine the zero-velocity of the template spectrum, we used the ULySS program (Koleva et al. 2009) with a medium spectral-resolution MILES library to simultaneously determine the line-of-sight velocity for the star, and its T_{eff} , $\log g$ and $[\text{Fe}/\text{H}]$. A fit over the $4160\text{--}5000 \text{ \AA}$ wavelength range finds a redshift of $cz = 320.7 \pm 0.7 \text{ km s}^{-1}$ (with a dispersion of $58.9 \pm 1.2 \text{ km s}^{-1}$). The stellar model fitting method also provides a best fit to the atmospheric properties of the star, finding an effective temperature of $T_{\text{eff}} = 36351 \pm 53 \text{ K}$, a surface gravity $\log g = 3.4 \pm 0.1$ [$\log(\text{cm s}^{-2})$], and a metallicity of $[\text{Fe}/\text{H}] = 0.25 \pm 0.01$.

This is compatible with an OIII type star, though the values are lower than those of an O5 III star in, for example, Martins et al. (2005). However, the exclusion of parts of the Balmer lines prevents us from undertaking more detailed stellar atmospheric modelling.

The final radial velocity, relative to the template, was calculated by performing the cross-correlation analysis in the $4150\text{--}4600 \text{ \AA}$ wavelength range which contains four He lines and the H γ line, and which has limited contamination from the sky lines and the nebula. The wavelength region $4343.5\text{--}4346.5 \text{ \AA}$ was ignored in the cross-correlation analysis as it contained significant contamination from a narrow nebula emission line superimposed on the stellar absorption line.

2.3 Orbital parameter determination

The binary orbital parameters were determined from the fit to the radial velocities using the HELIO_RV package which is part of the IDL Astronomy Library (Landsman 1993).² All reported errors on the fitted binary parameters are calculated by scaling the errors in the radial velocity measure-

² <https://idlastro.gsfc.nasa.gov/>

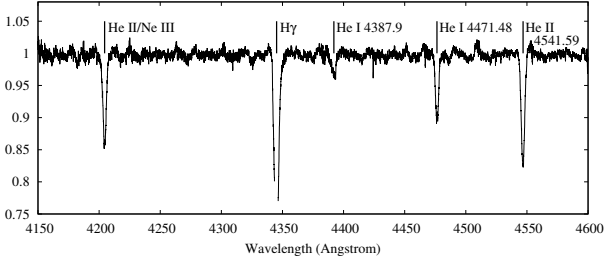


Figure 1. Template spectrum created from averaging over all observations. The gap in the H γ line is where a section was excluded from the cross-correlation calculation because of contamination by an emission line from the nebula.

ments to achieve a reduced χ^2 of exactly 1 (Lampton et al. 1976). This scaling factor was $\sim 1.2 - 5.2$ depending on the data. This does not change the values of the fitted parameters, but gives a more accurate estimate of the error, since additional systematic errors are better accounted for.

Table 1 shows the orbital parameters determined from the velocities of the individual lines. All fits were performed assuming a fixed period of 10.301 d. We find different velocities from the He I and He II lines, as was noted above. The measurements of the individual lines do suffer from lower signal-to-noise and for H β contamination from a nebula emission line.

The solution using the radial velocities determined from cross-correlation is shown in Table 2. If the orbital period is kept as a free parameter, the best-fitting orbital period is 10.314 ± 0.044 days, which is consistent with the 10.301 ± 0.002 d period found from the *Fermi*-LAT data (Corbet et al. 2016). However, searches for periodicity using the Lomb-Scargle technique could not detect a statistically significant period and we have, therefore, adopted an orbital period of 10.301 days for our final result.

We do note the systemic velocity we find, $\Gamma = 321.18 \pm 0.85$ km s $^{-1}$, is higher than the 295.8 ± 2.0 km s $^{-1}$ previously reported (Corbet et al. 2016). We undertook additional analysis to confirm that the wavelength calibration performed by the HRS pipeline was correct and that the comparison to the radial velocity standards was accurate to within the expected performance. We found no evidence of any discrepancy in the calibration, nor any long term systematic shift in the wavelength calibration over the period of observations. We believe that there are two possible reasons for this difference; there may be a possible systematic offset arising from the fit of the high resolution template fit to the medium resolution MILES libraries (however there is no significant offset to the radial velocity standards) or there may have been a systematic offset in the zero velocity in the field O-type star used in the previous analysis. However, this difference does not change the main results of determining the orbital parameters. If this difference in the systemic velocity is removed the radial velocities are in agreement with the previous results. The final radial velocity curve and the best-fitting model are shown in Fig. 2, and the data are given in Table 3. We find the binary is slightly eccentric, $e = 0.40 \pm 0.07$, and place the time of periastron at HJD 2457412.13 ± 0.29 .

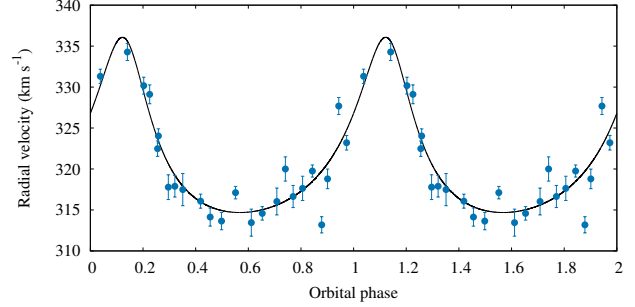


Figure 2. Radial velocity of the O5III star in the binary system, as determined from cross-correlation. The solid line shows the best fit to this data, with a fixed 10.301 day orbital period. For clarity the plot is reported over two orbital phases with phase $\phi = 0$ at MJD = 57 410.25, which corresponds to the given phase in Corbet et al. (2016). The error bars show the statistical errors reported by the RVSAO package.

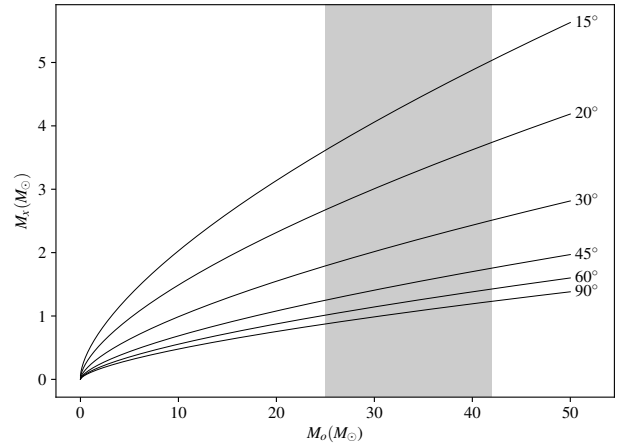


Figure 3. The constraint on the mass of the compact object in LMC P3. The shaded area marks the range of assumed masses of the optical companion.

3 DISCUSSION

3.1 Mass of the compact object

The binary parameter solution gives a mass function of $f = 0.0010 \pm 0.0004 M_{\odot}$ and the constraints on the mass of the compact object are shown in Fig. 3. The mass of an O5III(f) star is $\sim 40 M_{\odot}$ (Martins et al. 2005), but due to the binary evolution could be different. A mass range of $25 - 42 M_{\odot}$ was considered in Seward et al. (2012). For this mass range both a neutron star or black hole mass is compatible with the mass function, though a neutron star is favoured. For a $40 M_{\odot}$ star, the mass of the compact object will be $> 5 M_{\odot}$ for inclinations $i \leq 15 \pm 2^{\circ}$, and while the inclination must be $i \leq 11 \pm 1^{\circ}$ for a $25 M_{\odot}$ optical companion. Assuming the compact object is a pulsar, with a mass of $1.4 M_{\odot}$, the inclination will lie between $i = 39 \pm 6^{\circ}$ and $i = 59 \pm 11^{\circ}$ for a $25 M_{\odot}$ and $40 M_{\odot}$ star, respectively.

Table 1. Orbital parameters as determined from the radial velocities calculated by Gaussian fits to individual lines.

	H beta	He I 4471	He I 4921	He II 4541	He II 5411
Time of periastron (HJD)	2457412.15 ± 0.50	2457412.45 ± 0.21	2457411.89 ± 0.36	2457411.99 ± 0.21	2457412.14 ± 0.33
Orbital period (fixed, days)	10.301 ± 0.000	10.301 ± 0.000	10.301 ± 0.000	10.301 ± 0.000	10.301 ± 0.000
Systemic velocity (km/s)	298.43 ± 1.26	331.02 ± 0.75	335.95 ± 2.77	340.00 ± 0.48	337.33 ± 0.71
K (velocity semi-amplitude)	13.80 ± 2.84	15.14 ± 2.10	24.23 ± 26.31	11.30 ± 1.21	11.87 ± 1.68
Eccentricity	0.40 ± 0.12	0.52 ± 0.07	0.69 ± 0.28	0.42 ± 0.06	0.46 ± 0.08
Longitude of periastron (degrees)	5.9 ± 20.9	29.9 ± 10.4	354.5 ± 10.9	12.0 ± 8.9	8.1 ± 13.34
Mass function (M_{\odot})	0.0021 ± 0.0014	0.0023 ± 0.0010	0.0058 ± 0.0201	0.0011 ± 0.0004	0.0013 ± 0.0006

Table 2. Orbital parameters determined from the velocities calculated by cross-correlation. Note the systemic velocity is relative to the template file used.

Parameters	Free	Fixed (adopted)
Time of periastron (HJD)	2457411.77 ± 1.34	2457412.13 ± 0.29
Orbital period (days)	10.314 ± 0.044	10.301 ± 0.000
Systemic velocity relative to template (km/s)	0.73 ± 0.59	0.68 ± 0.55
Systemic velocity (km/s)	321.23 ± 0.88	321.18 ± 0.85
K (velocity semi-amplitude)	10.69 ± 1.24	10.69 ± 1.23
Eccentricity	0.39 ± 0.08	0.40 ± 0.07
Longitude of periastron (degrees)	12.9 ± 12.8	11.3 ± 12.0
Mass function (M_{\odot})	0.0010 ± 0.0004	0.0010 ± 0.0004

Table 3. Radial velocities obtained from cross-correlation

HJD	Radial velocity (km s ⁻¹)
2457655.60791	316.64 ± 1.35
2457665.60399	320.00 ± 1.48
2457691.50654	322.48 ± 0.94
2457708.46002	318.79 ± 1.20
2457711.56664	330.17 ± 1.03
2457722.44354	324.03 ± 0.87
2457723.39659	317.48 ± 1.96
2457724.46868	314.13 ± 1.11
2457725.46161	317.11 ± 0.76
2457728.46743	319.75 ± 0.74
2457730.47147	331.31 ± 0.87
2457731.53120	334.28 ± 1.04
2457732.40171	329.11 ± 1.15
2457733.38795	317.89 ± 1.32
2457734.39469	316.07 ± 0.86
2457736.37916	313.45 ± 1.65
2457737.37704	316.03 ± 1.64
2457738.38493	317.63 ± 1.48
2457774.33596	317.78 ± 1.51
2457776.41725	313.64 ± 1.06
2457780.33657	313.18 ± 0.99
2457781.31273	323.20 ± 0.89
2457788.31389	314.58 ± 0.82
2457791.30522	327.68 ± 1.04

3.2 Binary orientation

The orientation of the binary system is shown in Fig. 4. The system parameters are calculated assuming the optical star has a mass of $M_{\star} = 33.5 M_{\odot}$ and a radius of $R_{\star} = 14.5 R_{\odot}$ (average of the reported mass range and the corresponding average radius; e.g. Martins et al. 2005) and a mass of $M_p = 1.4 M_{\odot}$ for the compact object. This would correspond to

an inclination of $i \approx 50^{\circ}$. Following Corbet et al. (2016) phase $\phi = 0$ is assumed to be at MJD = 57410.25. Superior conjunction (when the compact object is behind the optical star) occurs at $\phi_{\text{sup}} = 0.98$ and inferior conjunction is at $\phi_{\text{inf}} = 0.24$ with periastron occurring at $\phi_{\text{per}} = 0.13$.

3.3 Implications for gamma-ray emission

The SALT HRS observations have shown that LMC P3 has an eccentricity of ≈ 0.4 and established the orientation (longitude of periastron) of the system. Both the eccentricity and the orientation play an important role in the modulation of the observed gamma-ray emission, since the inverse Compton scattering is dependent on the energy density of the target photons and the angle of scattering. In the cases of the highly eccentric systems PSR B1259–63/LS 2883 and PSR J2032+4127 gamma-ray emission is only detected near periastron (e.g. H.E.S.S. Collaboration et al. 2013; The VERITAS Collaboration et al. 2018).

The *Fermi*-LAT observations of LMC P3 show a flux, peaking slightly after phase $\phi \sim 0$ (Corbet et al. 2016) while the H.E.S.S. telescope has only detected the VHE emission, in a single phase bin of $\phi_{\text{bin}} = 0.2 - 0.4$ (HESS Collaboration et al. 2018). Such an out of phase light curve between the GeV and TeV gamma-ray emission can arise since $\gamma\gamma$ absorption can modulate very high energy emission (e.g. Dubus 2006; Böttcher & Dermer 2005). In this scenario, because of the strong angular dependence of inverse Compton scattering and $\gamma\gamma$ absorption, both the maximum in the inverse Compton emission and $\gamma\gamma$ absorption should occur around superior conjunction. This could lead to a maximum in the GeV light curve near superior conjunction since the photons are below the pair-production threshold energy, while the maximum in the TeV light curve will occur around inferior conjunction where the $\gamma\gamma$ opacity is lowest. The binary solu-

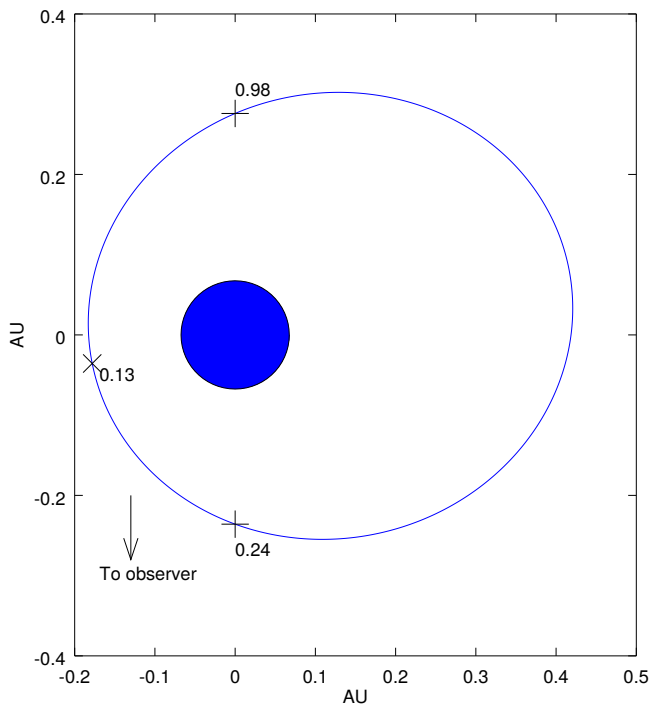


Figure 4. The binary orientation of the LMC P3. This is calculated assuming a $M_{\star} = 33.5 M_{\odot}$ and radius of $R_{\star} = 14.5 R_{\odot}$ and $M_p = 1.4 M_{\odot}$. The blue circle shows the relative size of the optical star while the black line traces the orbit of the compact object. The positions and orbital phase of superior and inferior conjunction are marked by + while the position and phase of periastron is marked by a x.

tion found in this paper supports this for the LMC P3, with superior conjunction lying at $\phi \approx 0.98$ at the peak of the *Fermi*-LAT light curve, while inferior conjunction, $\phi \approx 0.24$ is around the peak in the H.E.S.S. light curve.

Additionally Doppler boosting of the emission may play a role. The tail of the shock may obtain a relativistic bulk velocity, as is evident from hydrodynamical simulations of gamma-ray binaries (e.g. Bogovalov et al. 2008, 2012). If, due to $\gamma\gamma$ absorption, we predominately observe TeV gamma-ray emission originating from this region (with the GeV emission originating from the apex of the shock), this would lead to an enhancement in the observed TeV emission near inferior conjunction when the material is directed towards us (see e.g. Dubus et al. 2010; Zabalza et al. 2013).

4 CONCLUSION

We have undertaken SALT/HRS observations of LMC P3 and established the best orbital parameters for this system so far. The best-fitting solution shows the binary has an eccentricity of $e = 0.40 \pm 0.07$, which makes it similar to LS 5039. The best orbital parameter fit places superior conjunction at orbital phase $\phi = 0.98$, close to the maximum in the *Fermi*-LAT light curve, while inferior conjunction is at phase $\phi = 0.24$. This orientation may explain the anti-phase between the GeV and TeV light curves. The determined mass function, $f = 0.0010 \pm 0.0004 M_{\odot}$, favours a neu-

tron star compact object, and subsequently favours a pulsar wind driven and not accretion driven system.

ACKNOWLEDGEMENTS

The authors are grateful to P.A. Charles, A. Odendaal, A.F. Rajoelimanana and L.J. Townsend for valuable discussions. All of the observations reported in this paper were obtained with the Southern African Large Telescope (SALT). BvS and NK acknowledge that this work was supported by the Department of Science and Technology and the National Research Foundation of South Africa through a block grant to the South African Gamma-Ray Astronomy Consortium. AK and PV acknowledge the support of the National Research Foundation of South Africa.

REFERENCES

- Abdo A. A., et al., 2009, *Science*, **325**, 840
 Ackermann M., et al., 2016, *A&A*, **586**, A71
 Aharonian F., et al., 2005, *Science*, **309**, 746
 Bamba A., Ueno M., Nakajima H., Mori K., Koyama K., 2006, *A&A*, **450**, 585
 Bogovalov S. V., Khangulyan D. V., Koldoba A. V., Ustyugova G. V., Aharonian F. A., 2008, *MNRAS*, **387**, 63
 Bogovalov S. V., Khangulyan D., Koldoba A. V., Ustyugova G. V., Aharonian F. A., 2012, *MNRAS*, **419**, 3426
 Böttcher M., Dermer C. D., 2005, *ApJ*, **634**, L81
 Bramall D. G., et al., 2010, in *Ground-based and Airborne Instrumentation for Astronomy III*. p. 77354F, doi:10.1117/12.856382
 Bramall D. G., et al., 2012, in *Ground-based and Airborne Instrumentation for Astronomy IV*. p. 84460A, doi:10.1117/12.925935
 Buckley D. A. H., Swart G. P., Meiring J. G., 2006, in *Society of Photo-Optical Instrumentation Engineers (SPIE) Conference Series*. p. 62670Z, doi:10.1117/12.673750
 Casares J., Ribó M., Ribas I., Paredes J. M., Martí J., Herrero A., 2005, *MNRAS*, **364**, 899
 Corbet R. H. D., et al., 2016, *ApJ*, **829**, 105
 Crause L. A., et al., 2014, in *Ground-based and Airborne Instrumentation for Astronomy V*. p. 91476T, doi:10.1117/12.2055635
 Dubus G., 2006, *A&A*, **451**, 9
 Dubus G., 2013, *A&ARv*, **21**, 64
 Dubus G., Cerutti B., Henri G., 2010, *A&A*, **516**, A18
 Foellmi C., Moffat A. F. J., Guerrero M. A., 2003, *MNRAS*, **338**, 360
 H.E.S.S. Collaboration et al., 2013, *A&A*, **551**, A94
 HESS Collaboration et al., 2018, *A&A*, **610**, L17
 Ho W. C. G., Ng C.-Y., Lyne A. G., Stappers B. W., Coe M. J., Halpern J. P., Johnson T. J., Steele I. A., 2017, *MNRAS*, **464**, 1211
 Johnston S., Manchester R. N., Lyne A. G., Bailes M., Kaspi V. M., Qiao G., D’Amico N., 1992, *ApJ*, **387**, L37
 Kishishita T., Tanaka T., Uchiyama Y., Takahashi T., 2009, *ApJ*, **697**, L1
 Kniazev A. Y., Gvaramadze V. V., Berdnikov L. N., 2016, *MNRAS*, **459**, 3068
 Koleva M., Prugniel P., Bouchard A., Wu Y., 2009, *A&A*, **501**, 1269
 Kurtz M. J., Mink D. J., 1998, *PASP*, **110**, 934
 Lampton M., Margon B., Bowyer S., 1976, *ApJ*, **208**, 177

- Landsman W. B., 1993, in Hanisch R. J., Brissenden R. J. V., Barnes J., eds, *Astronomical Society of the Pacific Conference Series Vol. 52, Astronomical Data Analysis Software and Systems II*. p. 246
- Manick R., Miszalski B., McBride V., 2015, *MNRAS*, **448**, 1789
- Martins F., Schaerer D., Hillier D. J., 2005, *A&A*, **436**, 1049
- Mirzoyan R., Mukherjee R., 2017, *The Astronomer's Telegram*, **10971**
- Monageng I. M., McBride V. A., Townsend L. J., Kniazev A. Y., Mohamed S., Böttcher M., 2017, *ApJ*, **847**, 68
- Puls J., et al., 1996, *A&A*, **305**, 171
- Sarty G. E., et al., 2011, *MNRAS*, **411**, 1293
- Seward F. D., Charles P. A., Foster D. L., Dickel J. R., Romero P. S., Edwards Z. I., Perry M., Williams R. M., 2012, *ApJ*, **759**, 123
- The VERITAS Collaboration et al., 2018, preprint, p. [arXiv:1810.05271](https://arxiv.org/abs/1810.05271) ([arXiv:1810.05271](https://arxiv.org/abs/1810.05271))
- Waisberg I. R., Romani R. W., 2015, *ApJ*, **805**, 18
- Zabalza V., Bosch-Ramon V., Aharonian F., Khangulyan D., 2013, *A&A*, **551**, A17

This paper has been typeset from a $\text{\TeX}/\text{\LaTeX}$ file prepared by the author.